Reconfigurable localized-resonator valley topological acoustoelastic waveguides

Ting-Ting Wang[a], Bao-Long Chen[a], Kai Zhang[a,*], Yan-Feng Wang[b,*], Vincent Laude[c], Zi-Chen Deng[a], Yue-Sheng Wang[b,d]

[a] *School of Mechanics and Transportation Engineering, Northwestern Polytechnical University, 710072 Xi'an, China*
[b] *School of Mechanical Engineering, Tianjin University, 300350 Tianjin, China*
[c] *Université Marie et Louis Pasteur, CNRS, Institut FEMTO-ST, F-25000 Besançon, France*
[d] *Institute of Engineering Mechanics, Beijing Jiaotong University, 100044 Beijing, China*

Abstract

We employ a combined approach of numerical simulation and experimental validation to design a two-dimensional valley topological phononic crystal plate, in which cup-shaped cavities are connected to a perforated plate via thin beams and are arranged periodically. We systematically investigate the propagation characteristics of elastic waves in the phononic crystal plate featuring Valley-Hall edge states. Based on the principle of local resonance, low-frequency Dirac degeneracies are introduced. By modulating the volume of liquid in different resonators, the lattice symmetry is broken such that the energies of the upper and lower dispersion bands at the high-symmetry K point became unequal. This leads to the splitting of the Dirac cone degeneracy and to the formation of a topological bandgap, within which elastic wave propagation with topological protection is observed. Our work demonstrates topologically protected edge states propagating along interfacial boundaries between domains with distinct topological invariants. Furthermore, the acoustoelastic waveguides can be designed by selectively filling the liquid into the resonators, and the locally resonant frequencies can be continuously tuned by adjusting the liquid volume and concentration. Leveraging the concentration-dependent tuning of the resonant frequencies,

*Corresponding author.
Email addresses: kzhang@mwpu.edu.cn (Kai Zhang), wangyanfeng@tju.edu.cn (Yan-Feng Wang)

we develop a phononic crystal sensor for precise detection of liquid concentration. This study offers an innovative solution for reconfigurable acoustic devices, smart sensing systems, and elastic wave information processing technologies.

Keywords: Phononic crystal, Valley topological edge state, Local resonance, Reconfigurable waveguide, Tunable frequency

1. Introduction

Topological insulators originated from quantum wave systems [1] and due to their novel physical properties such as unidirectional transport and lossless energy propagation they have recently been extended to classical wave systems — including electromagnetic, acoustic, and elastic waves — thereby providing new paradigms for wave control [2, 3, 4, 5]. One widely studied example is the Valley-Hall insulator, which relies on the quantum valley Hall effect for topological transport, requiring neither to break time-reversal symmetry nor to rely on electron spin [6, 7, 8]. Moreover, the topological characteristics of the propagating waves are well preserved, rendering the system robust against defects and perturbations [9, 10, 11, 12].

Phononic crystals are a class of materials that achieve specific functionalities through the periodic arrangement of their internal structure [13, 14, 15]. One of their hallmark features is the ability to completely forbid the propagation of elastic waves within a certain frequency range, thereby creating a pronounced bandgap effect [16]. By modifying the shape, size, or material properties of the scatterers or matrix, or by adding or removing scatterers, the periodicity of an ideal phononic crystal can be locally disrupted to form various defects [17, 18]. In these defect regions, waves within the bandgap frequency ranges become confined and decay rapidly far away from the defects [19], making such structures highly suitable for both realizing and validating topological elastic wave states [20, 21, 22, 23]. Consequently, the valley topological phononic crystals, that combine Valley-Hall insulation with phononic crystal, hold significant potential for controlling elastic wave propagation, offering enormous prospects for the manipulation and application of elastic waves.

Valley topological phononic crystals rely on the design of their spatial structure for realization. By breaking the mirror [24, 25] or inversion [26, 27, 28, 29] symmetry of the lattice, the degeneracy of Dirac points in the

band structure is lifted, thereby establishing a Valley-Hall phase. At the interface between two crystals with opposite Valley-Hall phases, topologically protected valley edge states emerge, ensuring that elastic wave propagation remains robust against defects and sharp corners along the transmission path. A key objective in designing valley topological phononic crystals is to achieve a linear Dirac cone in the dispersion bands [30]. To date, numerous studies have demonstrated the guided propagation of acoustic or elastic waves along predetermined paths using such structures. Vila et al. designed a hexagonal lattice phononic crystal by arranging magnets at the corners of a hexagonal shelf to experimentally demonstrate that the topologically protected edge states exhibit minimal backscattering at sharp corners (>2 kHz) [20]. Huo et al. achieved a Valley-Hall phononic crystal by adjusting the size of the steel pillars to break spatial symmetry, demonstrating the robustness of the valley topological edge states under bending and defect conditions (>1 MHz) [31]. Lin et al. connected Y-shaped steel prisms to an aluminum plate to capture waves of different frequencies at various spatial locations, realizing a topological rainbow effect in elastic wave propagation (>10 kHz) [32]. However, most existing Valley-Hall designs rely on Bragg scattering-induced Dirac degeneracy, with the associated frequency determined by the lattice constant [33]. Consequently, achieving low-frequency topological transmission requires larger lattice dimensions, which may not be practical for many applications.

The design of valley topological phononic crystals based on local resonance fundamentally involves introducing local resonators into a lattice that satisfies C_{3V} symmetry to generate Dirac cones and the corresponding valley topological edge states [34, 35]. The Dirac cone appears just below the locally resonant bandgap, and its mode exhibits a pronounced low-frequency local resonance, indicating that the frequency of the Dirac cone is primarily determined by the locally resonant frequency [36]. Therefore, without altering the lattice constant, the position of the Dirac cone can be tuned by modifying the resonant frequency, enabling low-frequency elastic wave propagation along the valley topological edge state. To date, several studies have successfully demonstrated this approach. Zhang et al. employed heavy lead as the resonator to achieve low-frequency elastic wave propagation (<3 kHz) in valley topological phononic crystals [36]. Chen et al. utilized a similar structure to realize the valley locking effect for low-frequency elastic waves (<1 kHz) [37]. Although these locally resonant valley topological phononic crystals exhibit excellent wave control performance, their geometric shapes or

material parameters are typically fixed once fabricated, rendering the propagation paths of the edge states hardly reconfigurable and significantly limiting practical applications of elastic wave tuning. Thus, there is a pressing need to develop flexible and active control strategies for the frequency of the Dirac cone.

In recent years, there have been an increasing number of researches on tunable or active manipulation of wave propagation in valley topological phononic crystals, either by mechanical means or based on multifield coupling effects [38, 39, 40]. For example, edge states can be manipulated by embedding piezoelectric patches into phononic crystal unit cells and adjusting circuit parameters to modulate the effective Young's modulus or the density of the material [41]. However, piezoelectric tuning typically operates in the frequency range of tens of kHz to a few MHz. In the low-frequency regime, simulating the required giant inductance necessitates extremely bulky and power-consuming circuits. This not only increases system complexity and cost but also introduces issues related to high energy consumption and stability. Consequently, the practical engineering application of piezoelectric schemes is severely restricted at frequencies below 1 kHz. A programmable magnetic elevation array system has been applied to control the distribution of ferrofluid [42], thereby realizing a programmable valley topological phononic crystal for the modulation of elastic wave transmission paths. However, its operating frequency exceeds 1 kHz, and it fails to achieve continuous frequency tunability. Furthermore, generating a uniform magnetic field of sufficient intensity typically necessitates heavy electromagnetic coils or permanent magnet arrays, rendering the system extremely bulky. By applying a thermal field, frequency tuning of topologically protected edge states can be realized by exploiting the temperature sensitivity of material properties [43]. However, this method typically operates in the high-frequency range (hundreds of kHz). Furthermore, thermal inertia results in an extremely slow system response and significant energy consumption. For precise acoustic control, the presence of thermal gradients may also introduce unwanted inhomogeneity, thereby degrading the tuning precision of the system. For fluid-solid hybrid structures, the inherent fluidity and amorphous nature of the fluid facilitate the realization of reconfigurable phononic crystals. In particular, valley topological phononic crystals containing fluid scatterers in a solid matrix, which can be printed on-demand and reconfigured, can be good candidates for tunable waveguiding and sensing applications. Consequently, a reconfigurable valley topological phononic crystal device featuring

low-frequency operation, tunable transmission paths and frequencies, and operational simplicity can be realized.

In this work, we propose a valley topological phononic crystal that enables tuning of both the acoustoelastic waveguides and the low locally resonat frequencies of elastic waves (<1 kHz) based on the fluid-solid coupling. Specifically, resonators are constructed by connecting cup-shaped structures to a perforated plate via slender beams, and low-frequency Dirac degeneracies are introduced based on the principle of local resonance. By varying the amount of fluid filled into the cups, the mirror symmetry of the lattice is readily broken, thereby inducing Valley-Hall edge states. The reconfigurability of the phononic crystal structure is achieved through the selective distribution of fluid, which allows for the formation of acoustoelastic waveguides. We investigate the transmission characteristics of elastic waves along straight, L-shaped, Z-shaped, and forked paths. Furthermore, the frequency modulations of the valley topological edge states by changing the water level and the concentration of $MgSO_4$ solution in the resonators are explored. We also quantify the precise relationship between $MgSO_4$ solution concentration and the resonant frequency of the edge state, enabling the design of a phononic crystal sensor capable of accurately measuring solution concentration. Numerical simulations and experimental results exhibit excellent consistency, validating the proposed design and its capability for flexible control of low-frequency acoustoelastic wave propagation in valley topological phononic crystals.

2. Methods

The unit cell of the designed valley topological phononic crystal is shown in Fig. 1(a). The blue and gray regions represent the introduced fluid and the solid parts. Each unit cell contains two cup-shaped cavities which can be filled with a fluid, with each cavity functioning as a resonator. The geometric dimensions of the unit cell are $a = 100$ mm, $R = 24.5$ mm, $r_1 = 19$ mm, $r_2 = 21$ mm, $b = 3$ mm, $t = 2$ mm, $d = 4$ mm, $c = 50$ mm. h_1 and h_2 denote the heights of the fluid filled into the left and right cavities, respectively. The first Brillouin zone of the unit cell is illustrated in Fig. 1(b), where the green triangle represents the first irreducible Brillouin zone. The unit cell is then periodically repeated in a honeycomb lattice to form the phononic crystal plate, as depicted in Fig. 1(c).

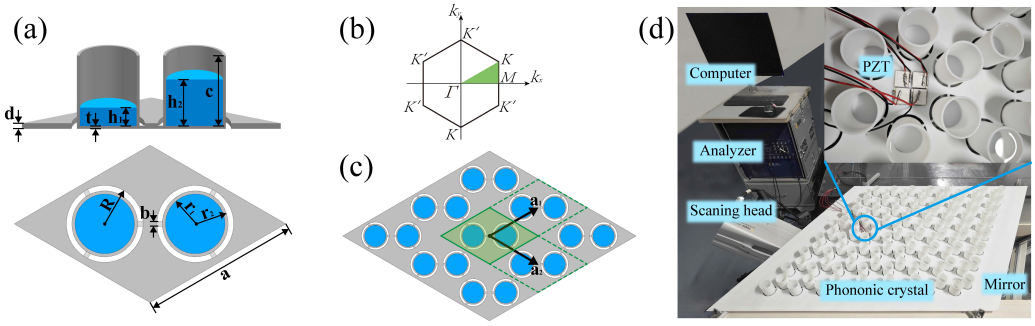

Figure 1: Structure of the valley topological phononic crystal and experimental setup. (a) Unit cell structure; (b) First Brillouin zone; (c) Periodic configuration of the supercell; (d) Experimental sample and setup.

The sample fabricated by the 3D printing is shown in Fig. 1(d). The solid material is epoxy, with density $\rho = 1130$ kg/m^3, Poisson's ratio $v = 0.42$, and Young's modulus $E = 2.65$ GPa. The fluids employed in this work include water and $MgSO_4$ solution. Water and $MgSO_4$ solution are nontoxic, harmless, inexpensive, and easily accessible, making them relatively ideal experimental materials. Water has a density of $\rho_w = 1000$ kg/m^3 and a sound speed $c_w = 1495$ m/s [44]. The densities of $MgSO_4$ solutions at 8%, 16%, and 24% (saturated) concentrations are 1.094 g/mL, 1.188 g/mL, and 1.282 g/mL, respectively [45, 46]. The sound speed in $MgSO_4$ solutions with different concentrations ranges from 1490 to 1800 m/s [47]. In the low frequency range, the acoustic wavelength in the fluid is much larger than the size of the cavities, so the sound speed does not significantly influence the experimental results [42]. The maximum mesh size in finite element simulations does not exceed 1/5-th of the wavelength.

Wave propagation is measured by a Polytec PSV-500 scanning vibrometer, with a periodic chirp selected as the source waveform. The vertical displacement vibration is detected by a vertically polarized piezoelectric patch bonded to the sample as shown in Fig. 1(d). The excitation region is a 40 $\times$ 40 mm square located at the input of the transmission paths, distributed symmetrically with respect to the topological interface. Laser light emitted by the PSV-500 scanning vibrometer is reflected by a mirror and directed onto the bottom surface of the phononic crystal plate, enabling the measurement of vibrations at every point on the underside of the plate. In the experimental setup, bandpass filters are employed according to the measure-

ment frequency range to reduce the influence of ambient noise on detection results. Finally, the acquired data are integrated using an analyzer to obtain the transmission spectrum and the displacement distributions.

To further evaluate the transmission characteristics of the system, the COMSOL Multiphysics software is used to conduct finite element analysis of the system. Based on Bloch's theorem, two-dimensional Bloch-Floquet periodic boundary conditions are applied onto pairs of opposite boundaries of the unit cell depicted in Fig. 1(a). When the cavities are filled with fluid, a soft acoustic boundary condition (with p=0) is imposed at the fluid–air interface. Interaction between fluid and solid, including the load exerted by the fluid on the solid structure and the influence of the acceleration on the fluid, is considered by applying a fluid-solid coupling boundary condition at the interface between fluid and solid. The boundary condition is as follows [48]:

$$-\mathbf{n}\cdot\left(-\frac{1}{\rho_c}\nabla p\right) = -\mathbf{n}\cdot\mathbf{u}_{tt}, \tag{1}$$

$$\mathbf{F}_A = p_t\mathbf{n}, \tag{2}$$

where $\mathbf{n}$ is the normal vector to the interface, ρ_c is the density of the fluid, p is the acoustic pressure, $\mathbf{u}_{tt}$ is the structural acceleration, $\mathbf{F}_A$ is the load exerted by the fluid on the structure, and p_t is the time-dependent acoustic pressure at the interface. Band structures are obtained using the eigenfrequency solver by sweeping the first irreducible Brillouin zone along the path ΓMKΓ, with the z-direction polarization D_z introduced to differentiate bands with different modes:

$$D_z = \frac{\iiint |w|^2\,dx\,dy\,dz}{\iiint \left(|u|^2+|v|^2+|w|^2\right)\,dx\,dy\,dz}, \tag{3}$$

where u, v, and w denote the displacement components along the x, y, and z directions respectively. It indicates that a dominant contribution of the vibrational displacement in the z-direction to the total displacement when the polarization approaches 1, signifying dominance of the out-of-plane wave.

The frequency response was calculated using the frequency domain solver. Low-reflective boundary conditions are implemented along the panel periphery to minimize unwanted reflections. For numerical simulation, a time-harmonic, spatially random wave source of vertical polarization is used at

the source region. This study focuses exclusively on out-of-plane wave propagation, i.e., vibrational components along the z-direction. Specifically, the transmission spectrum is then evaluated by sweeping the excitation frequency f with a normalized energy metric in decibel (dB) scale considering the ratio of integrated z-directional displacement components over the source and the receiver:

$$R(f) = 20 \log_{10} \left(\frac{\int_{S_r} U_z \, ds}{\int_{S_s} U_z \, ds} \right), \tag{4}$$

where U_z is the vertical displacement, S_s and S_r are the source and receiver areas respectively.

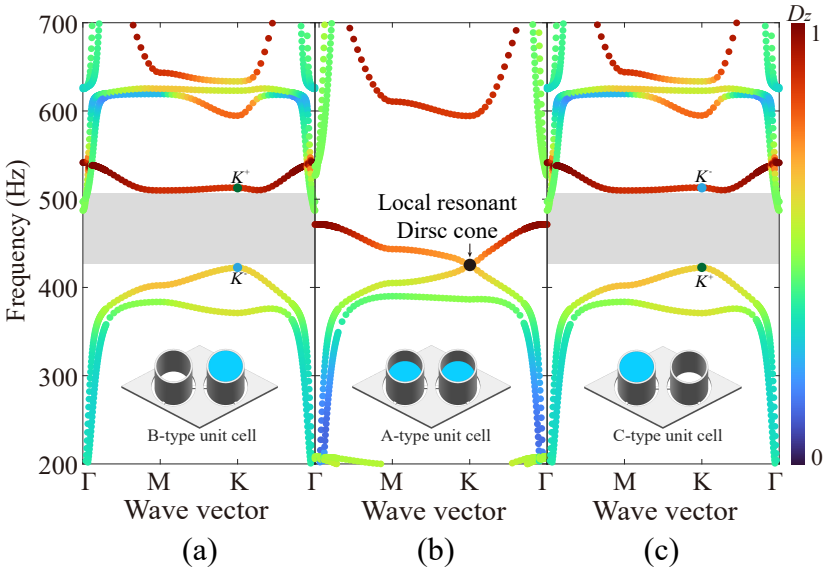

Figure 2: Band structures of unit cells with different heights of water. (a) B-type unit cell; (b) A-type unit cell; (c) C-type unit cell. The insets depict the corresponding unit cell models, and the color scale represents the polarization of the displacement in the z-direction.

The unit cell is referred to as the A-type unit cell when the heights of water in both resonant cavities are set to 25 mm. For the case that the left cavity is empty (0 mm) and the right cavity is fully filled with water (50 mm), the configuration is defined as the B-type unit cell. Conversely,

the C-type unit cell has the left cavity filled with water (50 mm) and the right cavity empty. The band structures for these three types of unit cells are shown in Fig. 2. In the A-type unit cell, the identical heights of water in the two cavities lead to the equal resonant frequencies preserving the spatial symmetry of the lattice. As a result, a degeneracy occurs at the high-symmetry K point (425 Hz), giving rise to a Dirac cone in the band structure illustrated in Fig. 2(b). In contrast, the mirror symmetries of the lattice are broken due to the asymmetric fluid distributions in the B-type and C-type unit cells. This symmetry breaking lifts the degeneracy at the K point and opens the Dirac cone, resulting in the bandgaps in the frequency ranges of 423–513 Hz as shown in Figs. 2(a) and 2(c). Although the band structures of B-type and C-type unit cell are nearly identical, a change in the topological phase occurs at the valley point K in the dispersion bands after the Dirac degeneracy. The valley Chern number is commonly used to evaluate topological phase transitions and to verify the existence of valley edge states. The valley Chern number can be expressed as:

$$C_{\mathrm{K}} = \frac{1}{2\pi} \int \Omega_n(\mathbf{k})\, d^2\mathbf{k}, \tag{5}$$

where $\Omega_n(\mathbf{k})$ denotes the Berry curvature of the nth band at a given wave vector $\mathbf{k}$, which can be expressed as:

$$\Omega_n(\mathbf{k}) = \nabla_{\mathbf{k}} \times \langle u_n(\mathbf{k}) | i\nabla_{\mathbf{k}} | u_n(\mathbf{k}) \rangle, \tag{6}$$

where $u_n(\mathbf{k})$ represents the periodic part of the displacement field in the unit cell corresponding to the wave vector $\mathbf{k} = (k_x, k_y)$, and $\langle u_n(\mathbf{k}) | i\nabla_{\mathbf{k}} | u_n(\mathbf{k}) \rangle$ denotes the Berry connection. The valley Chern number at the K^+ point (513 Hz) is +1/2, while it is -1/2 at the K^- point (423 Hz). The difference between the upper and lower branches is ± 1, indicating the emergence of a valley topological edge state within the band gap.

In order to study the relationship between the breaking of the spatial symmetry and the topological phase transition, we further investigate the relationship between the frequencies of the upper (red line) and lower (blue line) bands of the bandgap and the height difference of water ($\Delta h = h_1 - 25 = 25 - h_2$) filled in the two resonators, as shown in Fig. 3(a). The results indicate that the bandgap gradually becomes narrower as Δh decreases. When the heights of water in both resonators are equal, the bandgap completely disappears, resulting in a Dirac degeneracy. The phases at the K^+ and K^-

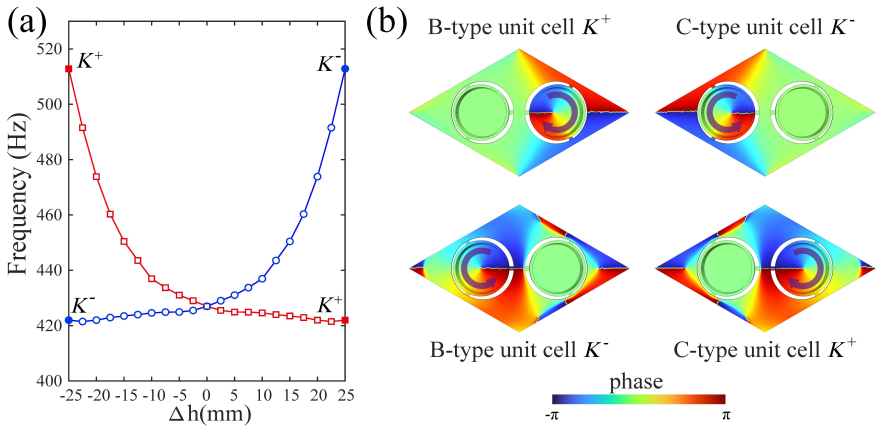

Figure 3: Topological phase transition analysis. (a) Relationship between the frequencies of the upper (red line) and lower (blue line) bandgap boundaries and the height difference Δh; (b) Phase distributions at the K^+ and K^- points for B-type and C-type unit cells. The purple arrows indicate the direction of the phase transition.

points for B-type and C-type unit cells are shown in Fig. 3(b), with the purple arrows indicating the direction of the phase transition. It can be observed that B-type and C-type unit cells exhibit the same direction of the phase transition at the K^+ (or K^-) points, indicating that a topological phase transition occurs upon lifting of the Dirac degeneracy.

Next, a supercell composed of B-type and C-type unit cells is cosidered to validate the existence of topological edge states within the frequency range of the locally resonant bandgap. The finite element model of the supercell is shown in Fig. 4(a), where five B-type and five C-type unit cells are periodically arranged on either side of the central interface. The two sides exhibit different topological phases. Periodic boundary conditions are applied to the long sides of the supercell and finite element analysis is conducted. It is observed in the band structure of the supercell that a continuous passing band emerges within the bandgap range from 423Hz to 513Hz that is formed by breaking the lattice symmetry as indicated by the red solid line in Fig. 4(b). From the z-polarized eigenmode at point A (473 Hz) on this band, shown in Fig. 4(c), it is observed that the displacement is symmetric relative to the interface with the z-direction vibration concentrating near the interface and decaying rapidly away from it. These results confirm that the continuous passing band corresponds to the valley topological edge state. Moreover, the maximum vibration displacement is observed in the resonators adjacent to

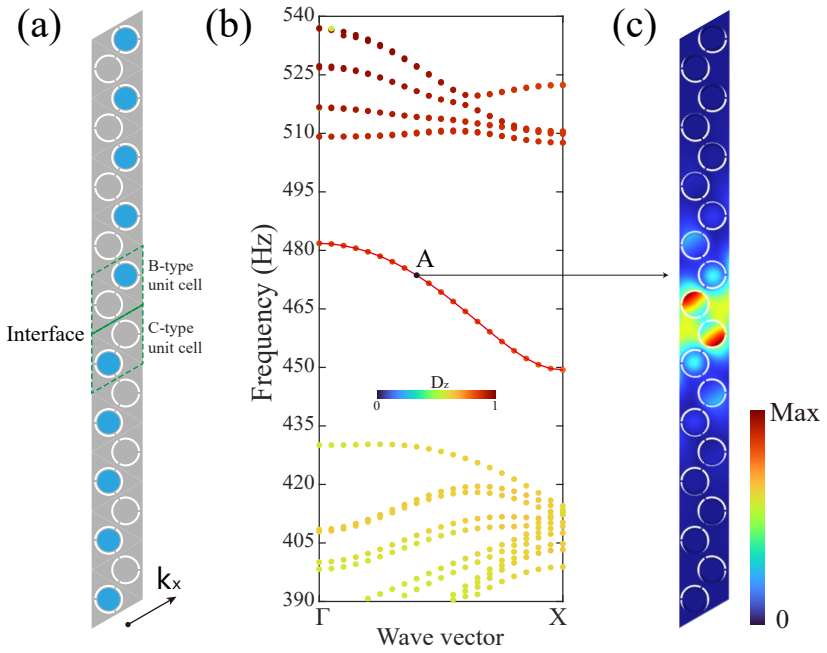

Figure 4: Topological edge states of the supercell composed of B-type and C-type unit cells. (a) Finite element model of the supercell; (b) Band structure of the supercell; (c) Eigenmodes of the supercell at point A.

the interface, which is attributable to the local resonance effect.

3. Results

3.1. Modulation of topological transmission acoustoelastic waveguides

Subsequently, the propagation of elastic waves along various topological transmission acoustoelastic waveguides is investigated by altering the location of water-filled resonators. By selectively filling water into the specific resonators while leaving the remaining ones empty, different topological waveguides including straight, L-shaped, Z-shaped, and seperated configurations can be constructed. The separated waveguides are further classified into types that either alter or maintain the wave propagation direction. Finite element models for the different transmission paths are illustrated in Figs. 5(a–e), where the excitation (black star) and receiver (red and green stars) positions are marked at the start and end of each transmission path.

By analyzing acoustoelastic wave propagation along these distinct topological paths, it is observed that strong resonant frequency peaks appear within the white shaded regions of the transmission spectra, while the transmission is rapidly decay in the gray shaded regions, as shown in Figs. 5(f–o). The frequency range of the white regions aligns well with the topological edge state identified in the supercell band structure shown in Fig. 4(b), indicating that acoustoelastic waves at the frequency of topological edge states are capable of propagating along different topological paths. The experimental transmission amplitudes are generally lower than those predicted by numerical simulation. The primary reason for this discrepancy is that the numerical simulation treats the phononic crystal as an idealized model, ignoring the inevitable energy dissipation present in the actual experimental environment. Specifically, factors such as the viscoelastic damping of the epoxy resin, the shear viscosity within the fluid, and the viscous friction at the fluid-structure interaction interface all contribute to energy loss. Additionally, it can be observed that the numerical transmission spectra exhibit multiple peaks, whereas the experimental curves are relatively smooth. This occurs because, under the undamped conditions of the numerical simulation, elastic waves undergo multiple reflections and coherent superposition within the finite domain. This leads to the formation of standing wave modes corresponding to the geometric dimensions of the plate, resulting in sharp peaks in the transmission curve. In contrast, when material viscosity is considered, elastic waves experience exponential decay during propagation. This attenuation disrupts the coherent superposition of multiple reflected waves, causing the transmission curve to become smoother [49, 50]. When the isotropic loss factor of the epoxy resin is estimated to be 0.03, the numerical transmission spectra of elastic waves along various paths are presented in the appendix. In this case, the simulation results show good agreement with the experimental spectra in terms of both transmission amplitude and number of peaks.

The numerical and experimental displacement field distributions at 465 Hz, shown respectively in Figs. 6(a–e) and 6(f–j), illustrate acoustoelastic wave propagation along different topological waveguides. It can be observed that vibrations are well confined near the designed acoustoelastic waveguides. Upon closer inspection, the displacement fields exhibit symmetric features with respect to the topological interfaces along the propagation paths. Simulation results show a good agreement with experimental observations. These findings validate that the proposed reconfigurable valley topological phononic crystal enables controlled routing of elastic waves by selectively

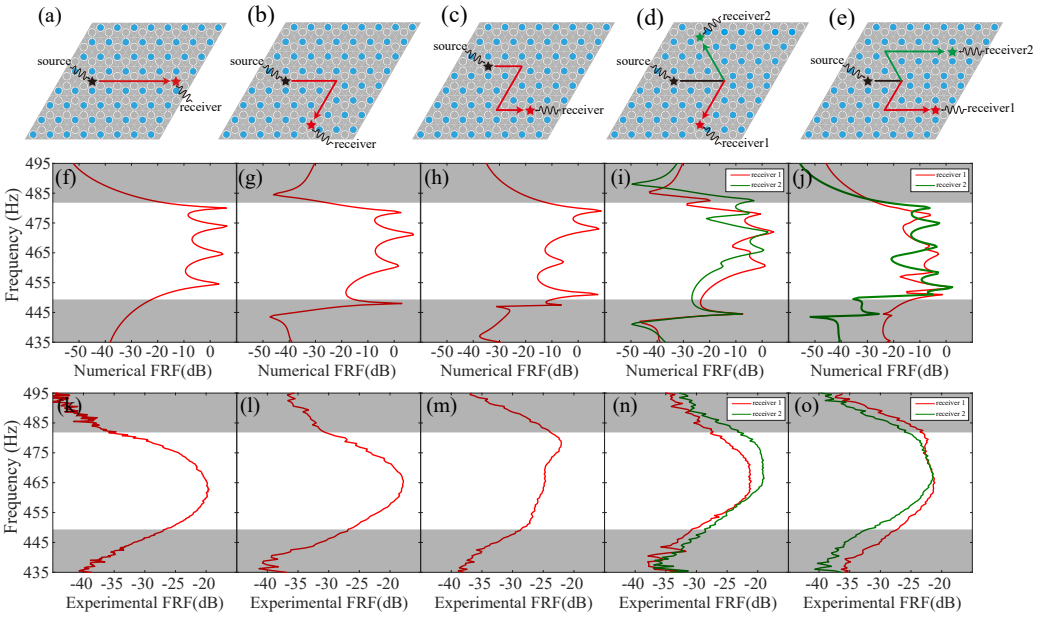

Figure 5: Elastic wave transmission characteristics along different topological acoustoelastic waveguides. (a) Straight; (b) L-shaped; (c) Z-shaped; (d) Seperated path with altered wave propagation direction; (e) Seperated path without a change in the propagation direction; (f)–(j) Numerical transmission spectra; (k)–(o) Experimental transmission spectra.

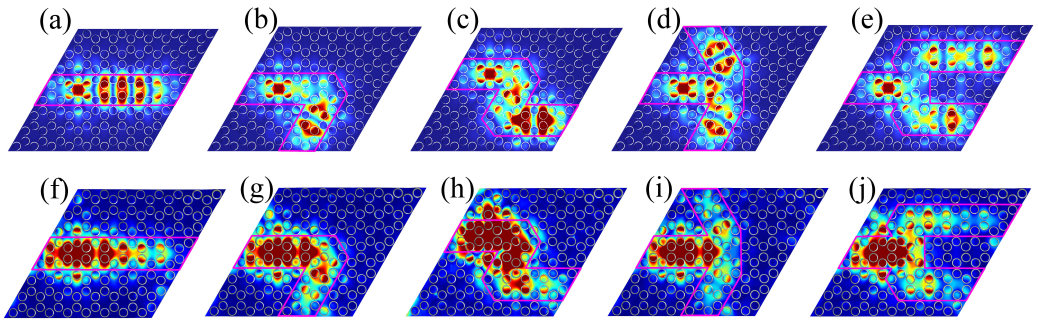

Figure 6: Displacement distribution of the phononic crystal with different topological acoustoelastic waveguides at 465 Hz. (a)-(e) Numerical displacement distribution; (f)-(j) Experimental displacement distribution. The color scale represents the amplitude of the z-direction vibration displacement.

filling different resonators with water to define various topological interface paths.

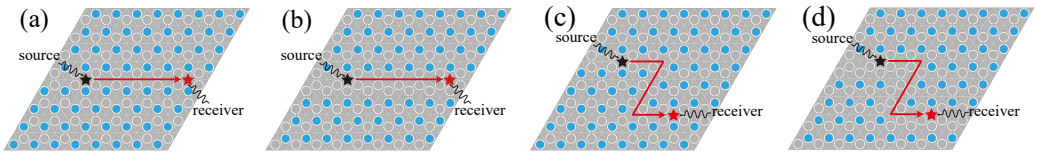

Figure 7: Topological and non-topological phononic crystals: (a) Straight topological waveguide;(b) Straight non-topological waveguide; (c) Z-shaped topological waveguide; (d) Z-shaped non-topological waveguide;

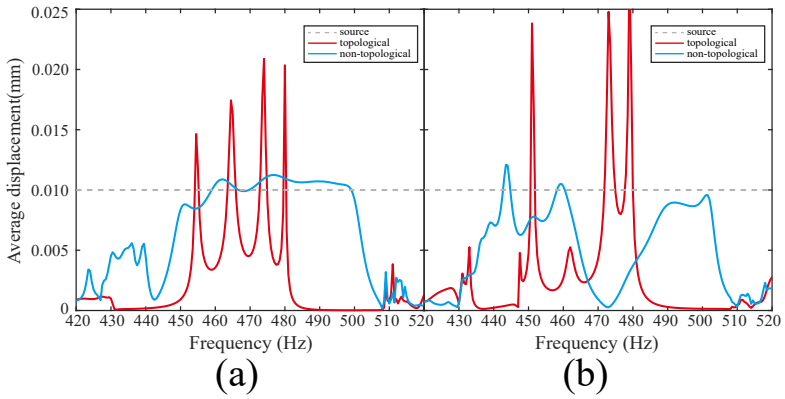

Figure 8: Comparison of numerical transmission between valley topological and non-topological phononic crystals: (a) Straight waveguides; (b) Z-shaped waveguides.

We further investigated the elastic wave transmission characteristics of valley topological and non-topological phononic crystals. The corresponding models are illustrated in Fig. 7(a-d). In the numerical simulations, a harmonic excitation with an amplitude of 0.01 mm was applied at the source region to calculate the average displacement amplitude at the receiving region for both straight and Z-shaped waveguides. Fig. 8 presents the frequency-dependent average displacement amplitudes at the receiver for valley topological and non-topological phononic crystals, where Fig. 8(a) corresponds to the straight transmission path and Fig. 8(b) to the Z-shaped path. In the plots, the dashed line indicates the displacement amplitude of the excitation source (0.01 mm). The red solid lines denote the average displacement amplitude at the receiver for the valley topological waveguides, while the blue solid lines represent that of the non-topological waveguides. As clearly observed from the figure, the valley topological waveguide (red solid line) exhibits significant advantages in signal amplification and transmission robustness com-

pared to the non-topological waveguide (blue solid line). Specifically, at the resonant frequencies of the topological edge states, the average displacement amplitude at the receiver of the valley topological waveguide presents sharp resonant peaks. Such narrow-bandwidth resonance characteristics are pivotal for sensing applications, as they significantly enhance the system's resolution and sensitivity to minute frequency shifts. Furthermore, these peaks far exceed the source excitation amplitude, demonstrating excellent energy localization and enhancement effects. Crucially, a comparison between the straight (Fig. 8(a)) and Z-shaped (Fig. 8(b)) waveguides reveals that, despite the introduction of multiple sharp corners in the Z-shaped path, the resonant peak amplitudes of the valley topological waveguide do not exhibit significant attenuation, maintaining highly efficient transmission. In contrast, the displacement at the receiver of the Z-shaped non-topological waveguide appears disordered with lower amplitudes, indicating severe backscattering losses at the bends. These results strongly confirm the topologically protected nature of the valley edge states, which enables stable and efficient elastic wave transmission even in complex paths.

3.2. Modulation of topological transmission by resonant frequencies

3.2.1. Changing the height of water

In addition to reconfiguring the topological transmission paths, the frequency of the topological edge states can also be tuned by adjusting the height of water in the resonators. Here, we investigate the effect of water level on the topological edge-state frequencies along both straight and Z-shaped topological paths, keeping empty resonators unchanged while setting the water height h in the filled resonators as either 32 mm, 38 mm, or 44 mm.

Taking the straight acoustoelastic waveguide as an example, the evolution of the topological edge-state dispersion of the supercell with different water heights is shown in Fig. 9(a). As h increases, the frequencies of the edge-state dispersion bands gradually decreases. The corresponding transmission spectra for acoustoelastic wave propagation along the straight path, obtained from numerical simulations and experimental measurements, are presented in Figs. 9(b) and 9(c), respectively. Both results clearly indicate that the resonant frequencies decrease with the increasing of the water height, and the resonant frequency ranges match well with the edge-state dispersion ranges in Fig. 9(a). Excellent agreement is observed between experimental and numerical results. The numerical and experimental displacement fields

for different water heights are displayed in Figs. 9(d)–(f) and Figs. 9(g)–(i), respectively. In all cases, vibrations remain well confined along the designed straight waveguide and the interface vibration modes exhibit mirror symmetry across the transmission interface, consistently with the topological edge-mode characteristics of the supercell. These results demonstrate that increasing the water height h effectively lowers the resonant frequencies of the topological edge states, thus enabling tunable topological transport of acoustoelastic waves along the straight waveguide.

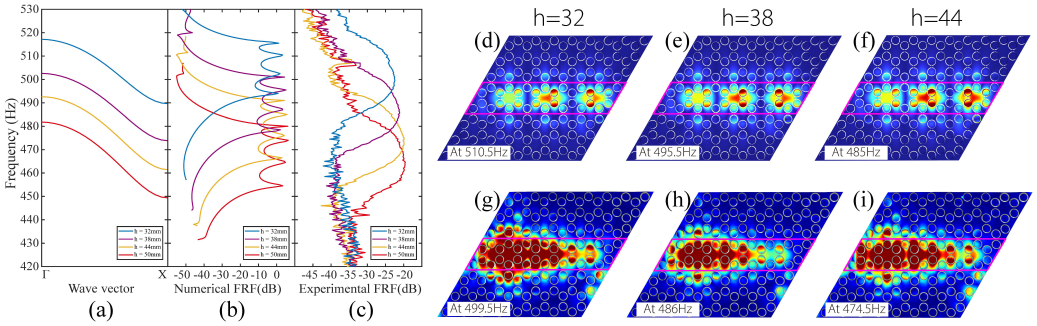

Figure 9: Transmission characteristics of elastic waves along the straight topological acoustoelastic waveguide with different heights of water. (a) Band structures; (b) Numerical transmission spectrum; (c) Experimental transmission spectrum; (d)-(f) Numerical displacement distributions; (g)-(i) Experimental displacement distributions.

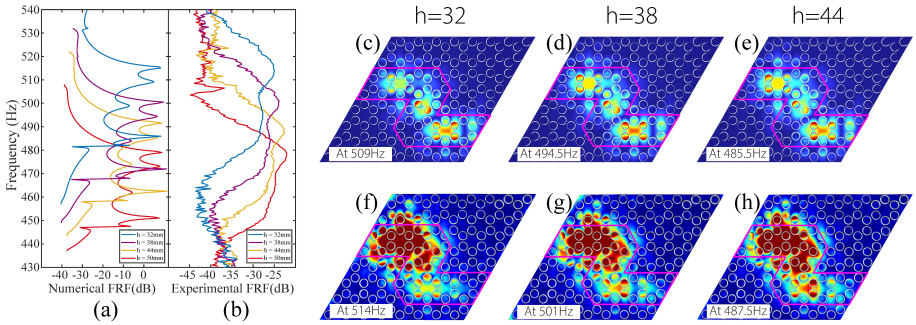

Figure 10: Transmission characteristics of elastic waves along the Z-shaped topological acoustoelastic waveguide with different heights of water. (a) Numerical transmission spectrum; (b) Experimental transmission spectrum; (c)-(e) Numerical displacement distributions; (f)-(h) Experimental displacement distributions.

For the Z-shaped topological acoustoelastic waveguide, it is not feasible to obtain the corresponding band structure. However, transmission spectra

can still be evaluated and compared. Numerical simulations and experimental measurements are shown in Figs. 10(a) and 10(b), respectively. Similar to the results for the straight case, the resonant peaks in the transmission spectra shift to lower frequencies as the water height h increases. This confirms that the tunability of acoustoelastic wave transmission through water height variation remains valid regardless of the specific transmission paths. The displacement fields for different water heights, obtained by numerical simulations and experiments, are shown in Figs. 10(c)–(e) and Figs. 10(f)–(h), respectively. In all cases, vibrations are well localized along the Z-shaped topological acoustoelastic waveguide.

The consistent frequency shift observed for both straight and Z-shaped paths demonstrates the effectiveness of tuning valley topological edge state frequencies by adjusting the water height in the resonators. Specifically, increasing the water height results in a downshift of the valley topological edge state frequency, whereas decreasing the water level shifts the frequency upward.

3.2.2. Changing the concentration of the $MgSO_4$ solution

Next, we investigate the tunability of the topological edge-state frequency by varying the concentration of the $MgSO_4$ solution filled in the resonators. Both straight and Z-shaped topological acoustoelastic waveguides are considered, with one set of resonators empty while the others are fully filled with a $MgSO_4$ solution to a height of 50 mm. The concentration of the $MgSO_4$ solution is set to either 8%, 16%, or 24% to examine the effect of fluid concentration on the topological edge-state frequencies.

First taking the straight transmission path as an example, Fig. 11(a) shows the evolution of the topological edge-state dispersion curves of the supercell for different $MgSO_4$ solution concentrations. It can be observed that the edge state frequencies gradually decrease as the fluid concentration increases. The numerical and experimental transmission spectra are shown in Figs. 11(b) and 11(c), respectively. With increasing solution concentration, the resonance peaks in the transmission spectra shift to lower frequencies and the frequency ranges remain consistent with those of the topological edge states shown in Fig. 11(a). The corresponding displacement fields obtained from numerical simulations and experiments are presented in Figs. 11(d)–(f) and Figs. 11(g)–(i), respectively. In all cases, vibrations remain well confined to the designed straight path and mode shapes exhibit definite symmetry along the interface, consistent with the supercell eigenmodes. These results

demonstrate that the edge state frequencies of elastic waves can be effectively tuned by adjusting the concentrations of the fluid in the resonators. Specifically, an increase in $MgSO_4$ solution concentration leads to a downshift of topological edge state frequencies, enabling frequency modulation of elastic wave transport along the straight topological acoustoelastic waveguide.

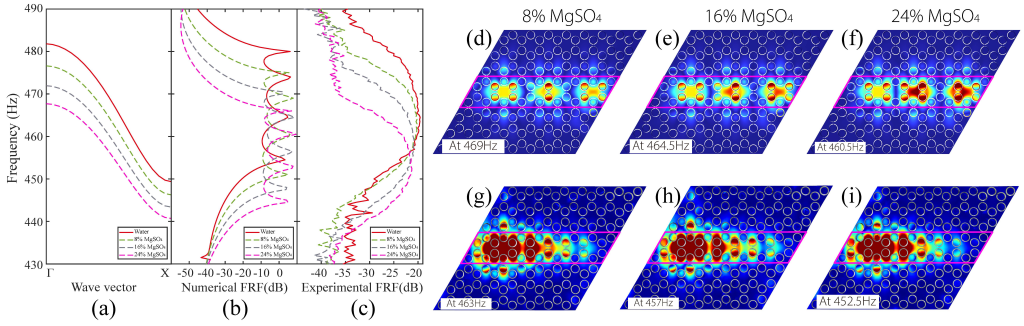

Figure 11: Transmission of elastic waves along a straight topological acoustoelastic waveguide filled with a $MgSO_4$ solution of varying concentration. (a) Band structures; (b) Numerical transmission spectrum; (c) Experimental transmission spectrum; (d)–(f) Numerical displacement distributions; (g)–(i) Experimental displacement distributions.

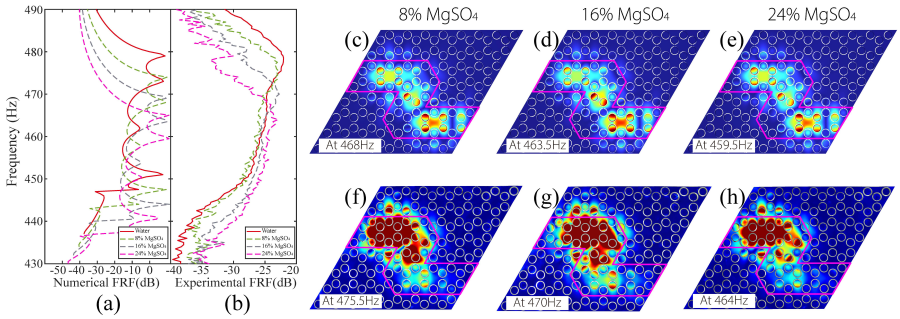

Figure 12: Transmission of elastic waves along the Z-shaped topological acoustoelastic waveguide filled with a $MgSO_4$ solution of varying concentrations. (a) Numerical transmission spectrum; (b) Experimental transmission spectrum; (c)–(e) Numerical displacement distributions; (f)–(h) Experimental displacement distributions.

Additionally, the variation of the transmission frequencies of topological edge states in Z-shaped phononic crystal plates filled with a $MgSO_4$ solution with varying concentration is considered. Numerical and experimental transmission spectra for acoustoelastic wave propagation along the Z-shaped path

are shown in Figs. 12(a) and 12(b), respectively. Consistent with the transmission behavior observed for the straight path configuration, the resonant frequencies in the transmission spectra of the Z-shaped path decrease with increasing $MgSO_4$ solution concentration and the corresponding frequency ranges agree well with those of the topological edge state dispersion curves shown in Fig. 11(a). This indicates that the capability to tune acoustoelastic wave transmission frequencies by altering the fluid concentration in the resonators is independent of the transmission path. From the numerical and experimental displacement fields shown in Figs. 12(c)–(e) and Figs. 12(f)–(h), respectively, it is observed that vibrations are well confined around the Z-shaped transmission path, and that modes exhibit symmetric characteristics along the interface which are consistent with those of the eigenmodes of the supercell. The consistent variation in edge state frequencies observed for both straight and Z-shaped topological acoustoelastic waveguides confirms that the frequencies of valley topological edge states can be effectively tuned by varying the fluid concentration inside the resonators. Specifically, an increase in fluid concentrations leads to a decrease in topological edge state frequencies, whereas a decrease in concentration results in a frequency increase.

From the perspective of physical mechanisms, an increase in the liquid volume or concentration within the resonator is equivalent to an enhancement of the system's effective mass. Based on the resonance theory of a spring-mass system, the resonant frequency f can be approximated as:

$$f = \frac{1}{2\pi}\sqrt{\frac{k}{m_{\text{eff}}}}, \tag{7}$$

where k denotes the equivalent stiffness and m_{eff} represents the effective mass of the system. As the water volume or solution concentration increases, the system's effective mass increases, thereby inducing a downward shift in the resonant frequency. This behavior is consistent with the experimental results observed in this work, where the frequency decreases with increasing water volume and solution concentration. This agreement further validates the physical feasibility of achieving frequency tunability by modulating the fluid effective mass.

3.3. Detection of $MgSO_4$ Solution Concentration

By varying the concentration of the $MgSO_4$ solution within the resonators, the frequencies of the topological edge states can be modulated. Conversely,

the phononic crystal can be used as a sensor for the concentration of the solution by detecting resonant frequencies. The relationship between resonant frequency and $MgSO_4$ concentration for the straight waveguide (Figs. 11 b–c) and Z-shaped waveguide (Figs. 12 a–b) are shown in Fig. 13(a) and 13(b), respectively. In the numerical simulations where damping is neglected, multiple resonant peaks appear. Here, the second highest resonance peak is chosen as the reference. It is worth noting that for the straight path (Figs. 13(a)), the numerical transmission peak frequency is lower than the experimental value. Conversely, for the Z-shaped path (Figs. 13(b)), the numerical peak frequency is higher than that observed in the experiment. Factors contributing to these discrepancies may include material inhomogeneity in the samples, geometric fabrication errors, damping-induced variations in wave propagation at the corners, and environmental influences such as water evaporation.

Linear fits to numerical and experimental data are shown with the blue and red dashed lines, respectively. These concentration and frequency relationships can be described by the following equations:

$$F_{\mathrm{S,Num}} = -0.56\,c + 473.75, \tag{8}$$

$$F_{\mathrm{S,Exp}} = -0.52\,c + 465.55, \tag{9}$$

$$F_{\mathrm{Z,Num}} = -0.56\,c + 472.75, \tag{10}$$

$$F_{\mathrm{Z,Exp}} = -0.61\,c + 479.35, \tag{11}$$

where $F_{\mathrm{S,Num}}$ and $F_{\mathrm{S,Exp}}$ are the numerical and experimental resonant frequencies for the straight waveguides, $F_{\mathrm{Z,Num}}$ and $F_{\mathrm{Z,Exp}}$ are the numerical and experimental resonant frequencies for the Z-shaped waveguides, and c is the concentration of the filling solution.

Equations (8)-(11) indicate that, for the straight waveguide, a 1% increase in $MgSO_4$ concentration results in a decrease of 0.56 Hz in the simulated resonant frequency and of 0.52 Hz in the experimental resonant frequency. For the Z-shaped waveguide, a 1% concentration increase results a 0.56 Hz reduction in the simulated resonant frequency and a 0.61 Hz reduction in the experimental resonant frequency. The coefficient of determination R^2 quantifies the goodness of the linear fit, with values closer to 1 indicating a better fit. The R^2 values for the four datasets are 0.9975, 0.9561, 0.9975, and 0.98, respectively, demonstrating a strong linear relationship between $MgSO_4$ concentrations and the resonant frequencies.

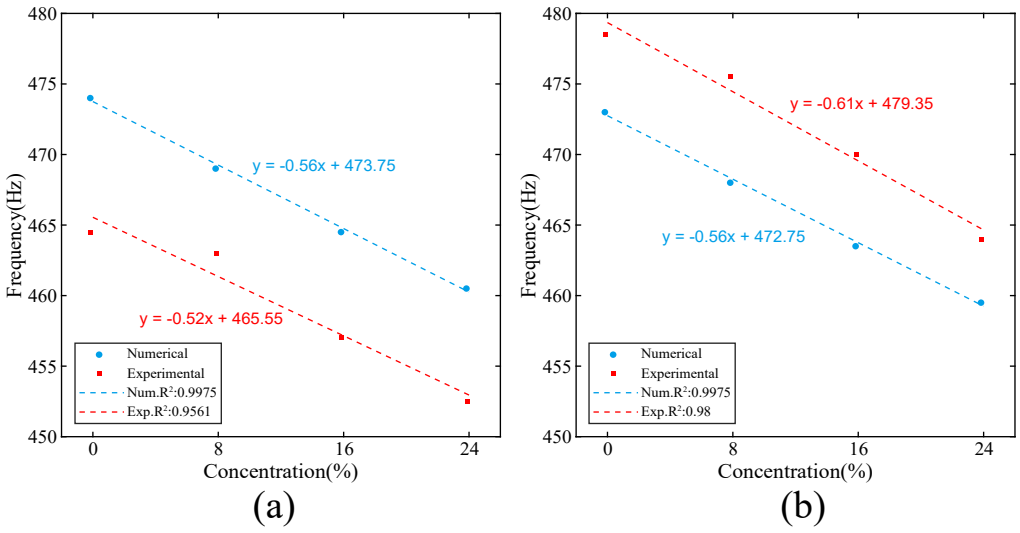

Figure 13: Relationship between resonant frequency and concentration of different $MgSO_4$ solutions: (a) Straight waveguide; (b) Z-shaped waveguide.

Next, we characterize the performance of the phononic crystal sensor based on several interrelated metrics. The quality factor Q quantifies the sharpness of the resonance and is defined as the ratio of the resonance frequency(f_r) to the full width at half maximum of the resonance peak ($\Delta f_{1/2}$) [51, 52]. A higher Q therefore indicates a better frequency resolution, which can be calculated by the following relationship:

$$Q = \frac{f_r}{\Delta f_{1/2}}. \tag{12}$$

Sensitivity S describes how much the resonant frequency shifts in response to a change in analyte concentration [53]. It reflects the frequency difference observed per unit change in concentration, which can be calculated by the following relation:

$$S = \frac{\Delta f}{\Delta c}, \tag{13}$$

where Δf is the difference of the transmission peak frequency between each concentration and zero concentration. Δc is the difference of the concentrations.

By combining the sensitivity S and the full width at half maximum of the resonance peak ($\Delta f_{1/2}$), the figure of merit (FOM) was defined as the ratio

of S to $\Delta f_{1/2}$—this reflects how strongly the sensor responds, which can be calculated by the following relation [54]:

$$\mathrm{FOM} = \frac{S}{\Delta f_{1/2}}. \tag{14}$$

Table 1: Performance metrics for phononic crystal sensors with straight waveguides

c (%)	f_r (Hz)		Sensitivity (Hz/%)		$\Delta f_{1/2}$ (Hz)		Q-factor		FOM	
	Num.	Exp.	Num.	Exp.	Num.	Exp.	Num.	Exp.	Num.	Exp.
0	474.0	464.5	–	–	31.35	31.00	15.12	14.98	–	–
8	469.0	463.0	0.625	0.188	29.35	31.00	15.98	14.94	0.02129	0.00605
16	464.5	457.0	0.594	0.469	28.35	31.80	16.38	14.37	0.02094	0.01474
24	460.5	452.5	0.563	0.500	27.15	25.70	16.96	17.61	0.02072	0.01946

Table 2: Performance metrics for phononic crystal sensors with Z-shaped waveguides

c (%)	f_r (Hz)		Sensitivity (Hz/%)		$\Delta f_{1/2}$ (Hz)		Q-factor		FOM	
	Num.	Exp.	Num.	Exp.	Num.	Exp.	Num.	Exp.	Num.	Exp.
0	473.0	478.5	–	–	35.35	42.95	13.38	11.14	–	–
8	468.0	475.5	0.625	0.375	33.50	38.90	13.97	12.22	0.01866	0.00964
16	463.5	470.0	0.594	0.531	32.00	40.75	14.48	11.53	0.01855	0.01304
24	459.5	464.0	0.563	0.604	30.85	35.90	14.90	12.93	0.01823	0.01683

The performance metrics of straight and Z-shaped phononic crystal sensors for different concentrations of $MgSO_4$ solutions are summarized in Table 1 and Table 2, respectively. All measured resonant frequencies exhibit a strong linear correlation with the $MgSO_4$ solution concentration, indicating that the proposed sensor demonstrates a good stability and reliability.

Table 3: Comparison of performance metrics with other reported works

Reference	Detection object	Working frequency	Sensitivity	Q-factor
Our work	$MgSO_4$ in water	452.5–478.5 Hz	0.62 Hz/%	17.61
Tong Zhu *et al.*[48]	NaCl in water	14–15 kHz	30.38 Hz/%	71.3
Fatma Khateib *et al.*[55]	Albumin in water	2.88–3.016 GHz	3.51 MHz/%	4308.57
Hamed Gharibi *et al.*[56]	Nal in water	82 610–83 530 Hz	1833 Hz/%	1300
Villa-Arango *et al.*[57]	Ethanol in water	1.1 MHz	–	–
Mukhin *et al.*[58]	Propanol in water	660–678 kHz	4 Hz /s^{-1}	600

This enables consistent detection of concentration variations across the entire range of $MgSO_4$ solution concentrations. However, it is worth noting that a slight differences in the resonant peak frequencies are observed between straight and Z-shaped waveguides. This discrepancy is likely attributed to additional geometric phase delays introduced as the elastic waves propagate through the bends, which modify the wave transmission behavior compared to that along a straight path. The comparison of performance parameters with other reported works are shown in table 3. The phononic crystal sensor proposed in this study establishes a sustainable and reusable detection platform. By simply replacing the liquid in the resonant cavity, users can achieve functional reconfiguration on the same physical structure, significantly reducing long-term operational costs. Unlike most existing works that focus on high-frequency sensing in the kHz, MHz, or even GHz ranges, this sensor operates in the low-frequency band of 452.5–478.5 Hz. This frequency range aligns well with ubiquitous environmental and industrial vibration sources, effectively avoiding the need for dedicated high-frequency excitation equipment typically required in ultrasonic sensing. Consequently, this device demonstrates greater potential for practical application. It is worth noting that Our work have elevated liquid concentration detection to the topological dimension. By leveraging the protection mechanism of valley topological edge states, the sensor is capable of performing concentration detection not only along straight paths but also along curved Z-shaped paths.

Despite the proposed phononic crystal sensor exhibiting a high quality factor and an excellent linear response in detecting $MgSO_4$ concentration, it faces certain limitations regarding practical application. First, the sensor's performance may be susceptible to environmental factors; specifically, since fluid density is temperature-dependent, thermal fluctuations could compromise the stability of the resonant frequency. Future iterations could incorporate integrated temperature control systems to enhance environmental adaptability. Second, experimental reproducibility is influenced by factors such as liquid evaporation, filling inconsistency, and minor deviations in the excitation source position, which may induce slight frequency shifts. To improve measurement reproducibility, future work could employ automated liquid handling systems and fixed excitation-reception setups. Furthermore, given the current sensitivity and resonance peak width, the detection limit for concentration changes is approximately 1%. While sufficient for general monitoring, the capability to resolve ultra-low concentration variations requires further improvement.

4. Conclusion

A reconfigurable valley topological phononic crystal capable of controlling both the propagation and the resonant frequencies of guided acoustoelastic waves is presented. Local resonance is considered to introduce a low-frequency Dirac degeneracy, that is subsequently lifted by modulating either the height or the concentration of fluids inserted inside the resonant cavities, inducing low-frequency valley topological edge states. By selectively filling a fluid into the specific resonators, both numerical simulations and experimental results demonstrate that elastic waves can be transmitted along various topological acoustoelastic waveguides, – including straight, L-shaped, Z-shaped, and separated configurations, – achieving reconfigurable control over elastic wave routing. Furthermore, by varying the height and concentration of the fluid filling the resonators, the resonance frequencies of the valley topological edge states can be tuned continously. Our results consistently show that an increase in the height of fluid or concentration leads to a decrease in the topological edge state frequency, whereas a decrease in these parameters conversely results in a frequency increase. Importantly, this tuning behavior is independent of the chosen topological acoustoelastic waveguide.

Exploiting the relationship between the resonance frequency and the concentration of different $MgSO_4$ solutions, we have further designed a phononic crystal sensor capable of accurately detecting the concentration of $MgSO_4$ solutions. The sensor structure proposed in this study exhibits excellent scalability and significant potential for system integration. By adjusting the geometric dimensions of the resonant cavity or the liquid filling volume, the sensor can be tailored to meet detection requirements across different frequency bands, enabling multi-parameter and multi-path sensing. Although this work focuses on $MgSO_4$ solutions, the sensor is equally applicable to other liquids exhibiting density-dependent concentration variations, providing a novel strategy for realizing acoustic sensing platforms that are low-cost, reconfigurable, and capable of low-frequency detection.

Acknowledgments

The authors acknowledge financial support by the National Key R&D Program of China (2024YFB3408700 and 2024YFB3408703) and the National Natural Science Foundation of China (12172297). Y.W. acknowl-

edges support by the Natural Science Foundation of Tianjin, China (20JC-QNJC01030). V.L. acknowledges financial support by the EIPHI Graduate School (ANR-17-EURE-0002).

Appendix. Numerical transmission spectra considering damping of the solid epoxy resin

To validate the impact of energy dissipation discussed previously, Figs. A1 (a)–(c) display the numerical transmission spectra calculated with an isotropic loss factor of $\eta = 0.03$ for the epoxy resin, which correspond sequentially to the phononic crystal waveguides in Figs. 5(a)–(e). By comparing Figs. A1 (a)–(c) with the experimental transmission spectra in Figs. 5(k)–(o), it is reveals that the introduction of damping significantly improves the agreement between the numerical predictions and the experimental measurements. Specifically, after accounting for damping, the numerical transmission curves exhibit attenuated amplitudes and a smoother profile, characterized by a single resonant peak within the topological edge state frequency range. The numerical results align closely with the experimental data in terms of peak amplitude, spectral smoothness, and the number of peaks. This indicates that an isotropic loss factor of 0.03 is a reasonable estimation, accurately reflecting the attenuation of elastic waves in the epoxy resin. Crucially, this result corroborates our previous explanation regarding the discrepancies observed in Fig. 5. It confirms that the sharp peaks and excessive amplitudes appearing in the undamped spectra were primarily artifacts arising from the neglect of dissipation.

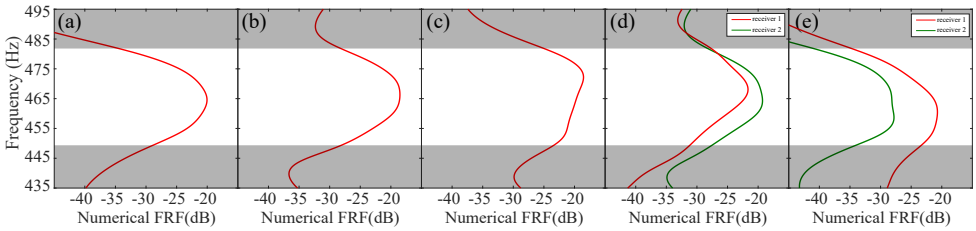

Figure A1: Numerical transmission spectra of elastic waves along various paths considering the damping of the epoxy resin (isotropic loss factor $\eta = 0.03$). (a) Straight; (b) L-shaped; (c) Z-shaped; (d) Seperated path with altered wave propagation direction; (e) Seperated path without a change in the propagation direction.

References

[1] D. J. Thouless, M. Kohmoto, M. P. Nightingale, M. den Nijs, Quantized hall conductance in a two-dimensional periodic potential, Physical review letters 49 (6) (1982) 405.

[2] F. D. M. Haldane, S. Raghu, Possible realization of directional optical waveguides in photonic crystals with broken time-reversal symmetry, Physical review letters 100 (1) (2008) 013904.

[3] M. Z. Hasan, C. L. Kane, Colloquium: topological insulators, Reviews of modern physics 82 (4) (2010) 3045–3067.

[4] Z. Wang, Y. Chong, J. D. Joannopoulos, M. Soljačić, Observation of unidirectional backscattering-immune topological electromagnetic states, Nature 461 (7265) (2009) 772–775.

[5] Z. Wang, Y. Chong, J. D. Joannopoulos, M. Soljačić, Reflection-free one-way edge modes in a gyromagnetic photonic crystal, Physical review letters 100 (1) (2008) 013905.

[6] A. Rycerz, J. Tworzydło, C. Beenakker, Valley filter and valley valve in graphene, Nature Physics 3 (3) (2007) 172–175.

[7] D. Xiao, W. Yao, Q. Niu, Valley-contrasting physics in graphene: magnetic moment and topological transport, Physical review letters 99 (23) (2007) 236809.

[8] H.-D. Song, D. Sheng, A.-Q. Wang, J.-G. Li, D.-P. Yu, Z.-M. Liao, Topological transport in dirac electronic systems: A concise review, Chinese Physics B 26 (3) (2017) 037301.

[9] Y. Chen, X. Liu, G. Hu, Topological phase transition in mechanical honeycomb lattice, Journal of the Mechanics and Physics of Solids 122 (2019) 54–68.

[10] N. Gao, S. Qu, L. Si, J. Wang, W. Chen, Broadband topological valley transport of elastic wave in reconfigurable phononic crystal plate, Applied Physics Letters 118 (6) (2021).

[11] Z.-G. Geng, Y.-G. Peng, Y.-X. Shen, D.-G. Zhao, X.-F. Zhu, Acoustic delay-line filters based on largely distorted topological insulators, Applied Physics Letters 113 (3) (2018).

[12] H. Fang, G. Xie, H. Huang, J. Chen, Coupled topological rainbow trapping of elastic waves in two-dimensional phononic crystals, Scientific Reports 14 (1) (2024) 17011.

[13] E. Yablonovitch, Inhibited spontaneous emission in solid-state physics and electronics, Physical review letters 58 (20) (1987) 2059.

[14] M. S. Kushwaha, P. Halevi, L. Dobrzynski, B. Djafari-Rouhani, Acoustic band structure of periodic elastic composites, Physical review letters 71 (13) (1993) 2022.

[15] W. Zhong, R. Cai, X. Zhuang, T. Rabczuk, Y. Pennec, B. Djafari-Rouhani, Y. Jin, Reconfigurable localized effects in non-hermitian phononic plate, Applied Physics Letters 122 (22) (2023) 222203.

[16] M. Sigalas, E. N. Economou, Band structure of elastic waves in two dimensional systems, Solid state communications 86 (3) (1993) 141–143.

[17] N. Gao, J. Li, R. Bao, W. Chen, Study of the band gaps of two dimensional phononic crystals with criss-crossed elliptical holes, Journal of Zhejiang University (Engineering Science), in press (in Chinese) (2019).

[18] S. Ning, D. Chu, F. Yang, H. Jiang, Z. Liu, Z. Zhuang, Characteristics of band gap and low-frequency wave propagation of mechanically tunable phononic crystals with scatterers in periodic porous elastomeric matrices, Journal of Applied Mechanics 88 (5) (2021) 051001.

[19] R. Anufriev, M. Nomura, Heat conduction engineering in pillar-based phononic crystals, Physical Review B 95 (15) (2017) 155432.

[20] J. Vila, R. K. Pal, M. Ruzzene, Observation of topological valley modes in an elastic hexagonal lattice, Physical Review B 96 (13) (2017) 134307.

[21] M. Yan, J. Lu, F. Li, W. Deng, X. Huang, J. Ma, Z. Liu, On-chip valley topological materials for elastic wave manipulation, Nature Materials 17 (11) (2018) 993–998.

[22] F. Schindler, A. M. Cook, M. G. Vergniory, Z. Wang, S. S. Parkin, B. A. Bernevig, T. Neupert, Higher-order topological insulators, Science advances 4 (6) (2018) eaat0346.

[23] M. Miniaci, R. Pal, B. Morvan, M. Ruzzene, Experimental observation of topologically protected helical edge modes in patterned elastic plates, Physical Review X 8 (3) (2018) 031074.

[24] J. Zhao, Q. Wang, X. Wang, W. Yuan, Y. Huang, S. Chen, A. Riaud, J. Zhou, On-chip valley phononic crystal plates with graded topological interface, International Journal of Mechanical Sciences 227 (2022) 107460.

[25] K. Tang, M. Makwana, R. V. Craster, P. Sebbah, Observations of symmetry-induced topological mode steering in a reconfigurable elastic plate, Physical Review B 102 (21) (2020) 214103.

[26] T.-W. Liu, F. Semperlotti, Synthetic kramers pair in phononic elastic plates and helical edge states on a dislocation interface, Advanced Materials 33 (9) (2021) 2005160.

[27] L. Yang, K. Yu, B. Bonello, B. Djafari-Rouhani, W. Wang, Y. Wu, Abnormal topological refraction into free medium at subwavelength scale in valley phononic crystal plates, Physical Review B 103 (18) (2021) 184303.

[28] S.-y. Huo, J.-j. Chen, H.-b. Huang, Y.-j. Wei, Z.-h. Tan, L.-y. Feng, X.-p. Xie, Experimental demonstration of valley-protected backscattering suppression and interlayer topological transport for elastic wave in three-dimensional phononic crystals, Mechanical Systems and Signal Processing 154 (2021) 107543.

[29] S.-Y. Huo, H.-B. Huang, C.-M. Fu, J.-J. Chen, Ideal type-ii weyl phases and surface states for elastic waves in three-dimensional solid phononic crystals, Physica Scripta 96 (12) (2021) 125714.

[30] Y. Jin, R. Wang, H. Xu, Recipe for dirac phonon states with a quantized valley berry phase in two-dimensional hexagonal lattices, Nano letters 18 (12) (2018) 7755–7760.

[31] S.-y. Huo, J.-j. Chen, H.-b. Huang, G.-l. Huang, Simultaneous multi-band valley-protected topological edge states of shear vertical wave in two-dimensional phononic crystals with veins, Scientific reports 7 (1) (2017) 10335.

[32] J. Lin, Y. Qi, Z. He, R. Bi, K. Deng, Topological rainbow trapping of elastic waves in two-dimensional valley phononic crystal plates, Applied Physics Letters 124 (8) (2024).

[33] G.-H. Li, Y.-Z. Wang, Y.-S. Wang, Active control on switchable waveguide of elastic wave metamaterials with the 3d printing technology, Scientific reports 9 (1) (2019) 16226.

[34] Y. Chen, D. Liu, Y. Wu, P. Yu, Y. Liu, Valley hall elastic topological insulator with large chern numbers, International Journal of Mechanical Sciences 239 (2023) 107884.

[35] W. Fang, C. Han, Y. Chen, Y. Liu, Valley hall elastic edge states in locally resonant metamaterials, Materials 15 (4) (2022) 1491.

[36] Q. Zhang, Y. Chen, K. Zhang, G. Hu, Dirac degeneracy and elastic topological valley modes induced by local resonant states, Physical Review B 101 (1) (2020) 014101.

[37] K. Chen, X. Dong, P. Gao, J. Zhang, Y. Sun, G. Tu, Z. Peng, Multifunctional applications of topological valley-locked elastic waves, International Journal of Mechanical Sciences 259 (2023) 108589.

[38] Z. Ma, Y. Liu, Y.-X. Xie, Y.-S. Wang, A simple elastic phononic crystal plate with adjustable topological valley transmission paths, Extreme Mechanics Letters 57 (2022) 101910.

[39] Y. Chen, B. Wu, J. Li, S. Rudykh, W. Chen, Low-frequency tunable topological interface states in soft phononic crystal cylinders, International Journal of Mechanical Sciences 191 (2021) 106098.

[40] L. Yao, D. Zhang, K. Xu, L. Dong, X. Chen, Topological phononic crystal plates with locally resonant elastic wave systems, Applied Acoustics 177 (2021) 107931.

[41] J. Zhou, J. Zhang, J. Chang, Z.-Y. Li, D. Yan, Active control topological valley modes in metamaterial plates, Crystals 13 (6) (2023) 933.

[42] Q. Zhang, Y. Chen, K. Zhang, G. Hu, Programmable elastic valley hall insulator with tunable interface propagation routes, Extreme Mechanics Letters 28 (2019) 76–80.

[43] H. Liu, S.-y. Huo, L.-y. Feng, H.-b. Huang, J.-j. Chen, Thermally tunable topological edge states for in-plane bulk waves in solid phononic crystals, Ultrasonics 94 (2019) 227–234.

[44] T.-T. Wang, Y.-F. Wang, Z.-C. Deng, V. Laude, Y.-S. Wang, Reconfigurable coupled-resonator acoustoelastic waveguides in fluid-filled phononic metaplates, Composite Structures 303 (2023) 116355.

[45] E. Ruiz-Agudo, F. Mees, P. Jacobs, C. Rodriguez-Navarro, The role of saline solution properties on porous limestone salt weathering by magnesium and sodium sulfates, Environmental geology 52 (2007) 269–281.

[46] G. Parmoon, A. Mohammadi Nafchi, M. Pirdashti, Density, viscosity, refractive index and excess properties of binary and ternary solutions of poly (ethylene glycol), sulfate salts and water at 298.15 k, Physical Chemistry Research 7 (4) (2019) 859–884.

[47] C.-T. Chen, L.-S. Chen, F. J. Millero, Speed of sound in nacl, mgcl2, na2so4, and mgso4 aqueous solutions as functions of concentration, temperature, and pressure, The Journal of the Acoustical Society of America 63 (6) (1978) 1795–1800.

[48] T. Zhu, T.-T. Wang, H.-T. Zhou, Y.-F. Wang, Y.-S. Wang, Reconfigurable phononic crystal sensor for liquid detection, Smart Materials and Structures 33 (3) (2024) 035016.

[49] A. Gueddida, Y. Pennec, V. Zhang, F. Lucklum, M. Vellekoop, N. Mukhin, R. Lucklum, B. Bonello, B. Djafari Rouhani, Tubular phononic crystal sensor, Journal of Applied Physics 130 (10) (2021) 105103.

[50] H. J. Lee, J. K. Lee, Y. Y. Kim, Elastic metamaterial-based impedance-varying phononic bandgap structures for bandpass filters, Journal of Sound and Vibration 353 (2015) 58–74.

[51] N. Mukhin, M. Kutia, A. Aman, U. Steinmann, R. Lucklum, Two-dimensional phononic crystal based sensor for characterization of mixtures and heterogeneous liquids, Sensors 22 (7) (2022) 2816.

[52] P. Xu, J. Zheng, J. Zhou, Y. Chen, C. Zou, A. Majumdar, Multi-slot photonic crystal cavities for high-sensitivity refractive index sensing, Optics express 27 (3) (2019) 3609–3616.

[53] A. M. Ahmed, A. Mehaney, Ultra-high sensitive 1d porous silicon photonic crystal sensor based on the coupling of tamm/fano resonances in the mid-infrared region, Scientific reports 9 (1) (2019) 6973.

[54] M. Zaremanesh, L. Carpentier, H. Gharibi, A. Bahrami, A. Mehaney, A. Gueddida, R. Lucklum, B. Djafari-Rouhani, Y. Pennec, Temperature biosensor based on triangular lattice phononic crystals, APL Materials 9 (6) (2021).

[55] F. Khateib, A. Mehaney, R. M. Amin, A. H. Aly, Ultra-sensitive acoustic biosensor based on a 1d phononic crystal, Physica Scripta 95 (7) (2020) 075704.

[56] H. Gharibi, A. Mehaney, A. Bahrami, High performance design for detecting nai–water concentrations using a two-dimensional phononic crystal biosensor, Journal of Physics D: Applied Physics 54 (1) (2020) 015304.

[57] S. Villa-Arango, R. Torres, P. Kyriacou, R. Lucklum, Fully-disposable multilayered phononic crystal liquid sensor with symmetry reduction and a resonant cavity, Measurement 102 (2017) 20–25.

[58] N. Mukhin, M. Kutia, A. Oseev, U. Steinmann, S. Palis, R. Lucklum, Narrow band solid-liquid composite arrangements: Alternative solutions for phononic crystal-based liquid sensors, Sensors 19 (17) (2019) 3743.